photonics

Communication

Integrated Broadband Filter with Sharp Transition Edges Based on SiN and SiON Composite Waveguide Coupler

Xiao Ma [1,*], Qiongchan Shao [2], Jiamei Gu [2], Tingting Lang [1], Xiang Guo [1] and Jian-Jun He [2]

[1] School of Information and Electronic Engineering, Zhejiang University of Science and Technology, Hangzhou 310023, China; langtingting@zust.edu.cn (T.L.); xiangguo@zust.edu.cn (X.G.)
[2] College of Optical Science and Engineering, Zhejiang University, Hangzhou 310027, China; shaoqiongchan@zju.edu.cn (Q.S.); gu_jiamei@zju.edu.cn (J.G.); jjhe@zju.edu.cn (J.-J.H.)
* Correspondence: maxiao@zust.edu.cn

Abstract: Broadband filters with sharp transition edges are important elements in diverse applications, including Raman and fluorescence spectral analysis, wideband wavelength-division multiplexing (WDM), and multi-octave interferometry. While the multi-layer thin-film interference broadband filter has been widely applied in various free-space optical systems, its integrated counterpart is still far from mature, which is also highly desired for constructing chip-scale miniature optical modules. In this article, we design, fabricate, and characterize an integrated broadband filter with sharp transition edges. An adiabatic coupler based on silicon nitride (SiN) and silicon oxynitride (SiON) composite waveguide is employed here. Long-pass, short-pass, band-pass, and band-stop filters can be realized in a single design of the composite waveguide coupler for a specific wavelength range, with only a difference in the SiN taper waveguide width. Experimental results with a roll-off value of larger than 0.7 dB nm^{-1} and a 15 dB extinction ratio (ER) are presented.

Keywords: integrated broadband filter; SiON waveguide; adiabatic coupler

check for updates

Citation: Ma, X.; Shao, Q.; Gu, J.; Lang, T.; Guo, X.; He, J.-J. Integrated Broadband Filter with Sharp Transition Edges Based on SiN and SiON Composite Waveguide Coupler. *Photonics* **2023**, *10*, 1285. https://doi.org/10.3390/photonics10111285

Received: 10 October 2023
Revised: 7 November 2023
Accepted: 16 November 2023
Published: 20 November 2023

1. Introduction

Photonic filters play a key role in integrated optics devices as fundamental building blocks. Their ability to selectively pass or stop different spectral bands is very important in various applications, including optical communication, interconnect, spectroscopy, and sensing [1–6]. In recent decades, numerous integrated filters with diverse structures have been proposed, such as arrayed waveguide grating (AWG), echelle diffraction grating (EDG), microring, microdisk, Bragg grating, photonic crystal (PC), Mach–Zehnder interferometer (MZI), directional coupler (DC), and so on [7–17]. By modifying their basic structures, employing new materials, and combining them, customized filtering performances required for specific applications can be achieved. For instance, a multi-order microring or a multi-stage MZI has a box-like filter response with a flat top and a sharp transition edge, which is indispensable for the WDM system [18,19]. Tunable filters constructed with lithium niobate on insulator (LNOI) show excellent electro-optic modulation efficiency and can function as an important component in tunable lasers and microwave photonics [20,21]. Thermal-tuned microring combined with thermal-tuned MZI constitutes a powerful spectral filter with both a wide spectral analysis range and a high optical resolution [22].

The majority of the above-mentioned filters are based on the theorem of two-beam or multi-beam interference. Despite exhibiting versatile capabilities, they can hardly achieve broadband filtering with sharp transition edges, which is a prerequisite for Raman and fluorescence spectral analysis, wideband WDM, and multi-octave interferometry. For example, grating filters, including Bragg grating [13,14], waveguide grating [17], EDG [9], AWG [1,7], and so on, are based on multi-beam interference. They can present a very sharp transition edge with a typical roll-off value of above 5 dB nm^{-1}; however, their filtering bandwidth is very small, and it is very difficult to exceed it beyond tens of nanometers. Although the multi-layer thin-film interference broadband filter has been widely applied in various commercial free-space optical systems, the building of a similar counterpart in integrated optics requires dozens of cascaded interference filters with finely designated filtering characteristics, posing an extremely difficult challenge for the fabrication process and can induce a large propagation loss.

Adiabatic waveguide couplers can also be used to construct filters. Ultra-broadband filters with passbands of thousands of nanometers have been developed [23,24]. However, due to the weak wavelength dependence of the coupling coefficient κ in the traditional adiabatic coupler design, a spectrum transits very slowly from the passband to the stopband. In Ref. [23] and Ref. [24], roll-off values of only 0.07 dB nm^{-1} and 0.04 dB nm^{-1} are reported. A chirped modulated adiabatic coupler originating from quantum theory has been proposed and simulated, showing a roll-off value of around 2 dB nm^{-1}. However, restricted by the modulation depth of the gap, its band-pass wavelength range cannot be very large [25]. Recently, E.S. Magden et al. demonstrated a transmissive silicon photonic dichroic filter exhibiting a wideband filtering ability with sharp transition edges [26,27] and roll-off values of 2.82 dB nm^{-1} and 0.64 dB nm^{-1} at 1550 nm, and 2100 nm bands were achieved [27]. In the filter, they designed an adiabatic coupler with the coupling coefficient κ, showing a strong wavelength dependence when employing a single-core and a three-segment silicon waveguide with distinctly different dispersion curves [27]. The large dispersion difference can be primarily attributed to the prominent refractive index difference between silicon and surrounding SiO_2. However, silicon has an absorption edge at 1100 nm; hence, it cannot be applied to a lower wavelength range, which is applicable to a number of important applications such as Raman and fluorescence spectral analysis.

In this article, we design, fabricate, and characterize an integrated broadband filter. An adiabatic coupler constituting SiN and SiON composite waveguide is employed here. As is well known, SiN has a relatively large refractive index of around 2, and SiON can vary its refractive index from 1.45 to 2. Both exhibit good stability and a large transmittance wavelength range from 300 nm to 2000 nm. Therefore, the composite waveguide made up of them shows the characteristics of high flexibility, reliability, and extensive applicability. Long-pass, short-pass, band-pass, and band-stop filters can be realized in a single design of the composite waveguide coupler for a specific wavelength range, with only a difference in the taper waveguide width. Experimental results with a roll-off value of larger than 0.7 dB nm^{-1} and an extinction ratio (ER) of 15 dB are presented here.

2. Theory and Design

A typical waveguide coupler is composed of two individual waveguides: A and B. If they are apart from each other by a far enough distance, mode fields φ_A and φ_B have no interference and can transmit independently with propagation constants of β_A and β_B, respectively. When the two waveguides become close, a supermode is created, and the power distribution between the two waveguides under weak coupling conditions can be described as follows [27]:

$$|T_A| = \frac{1}{2}\left(1 + \frac{\gamma}{\sqrt{1+\gamma^2}}\right) \tag{1}$$

where T_A represents the fraction of the total power lying in waveguide A. γ equals $\delta/|\kappa|$, in which δ is $(\beta_A - \beta_B)/2$, and κ is the coupling coefficient between the two waveguides. Equation (1) indicates that the power distribution in a supermode depends on the propagation constant difference δ and coupling coefficient κ. If δ equals 0, light in the two waveguides has equal power. The larger the δ and the smaller the $|\kappa|$, the more light will stay in waveguide A. In an adiabatic coupler, the rate of change of δ with the wavelength can determine the transition efficiency from the passband to the stopband or vice versa. A larger change rate leads to a sharper transition edge, and the key to obtaining a large change rate of δ is to ensure that waveguides A and B have distinctly different dispersion curves. This can be achieved through the use of waveguides made up of different materials or different structures.

In the study conducted by E.S. Magden et al., a three-segment silicon waveguide was utilized to create a significant dispersion contrast compared to the single-core channel silicon waveguide [27]. As we will discuss further, this structure is highly effective when the device needs to be fabricated using a single material. However, if we can find some different materials that can be combined without posing significant fabrication challenges, the composite waveguide structure appears more appealing due to its ability to present a greater dispersion contrast. Figure 1 illustrates four different waveguides that can be employed to construct an adiabatic waveguide coupler. The top left depicts a single-core SiN channel waveguide surrounded by SiO_2 with a refractive index of 1.444 as the envelope layer. The bottom left showcases a single-core SiON waveguide, while the right sections feature three-segment and five-segment SiN waveguides. The refractive indexes of SiN and SiON employed here are 1.98 and 1.6, respectively, at 1550 nm. The dispersion curves of the four waveguides are presented in Figure 2, with all waveguides designed to have the same effective indices at 1550 nm. From the figure, it is evident that the single-core SiN waveguide exhibits a much steeper dispersion curve than the SiON waveguide because of its larger refractive index. Both the three-segment and five-segment SiN waveguides can reduce the dispersion, and when the duty cycles are set to 80%, the largest dispersion contrast can be achieved. This is attributed to the multi-segment SiN waveguides allocating more power in the gap area with a low refractive index, thereby displaying a neutralized dispersion curve between SiN and SiO_2. However, compared with the single-core SiON waveguide, the slopes of their dispersion curves are still too large. Therefore, based on Equation (1), the single-core SiN waveguide and single-core SiON waveguide, which exhibit the largest dispersion contrast, are most suitable for constituting the adiabatic-coupler-based broadband filter with sharp transition edges.

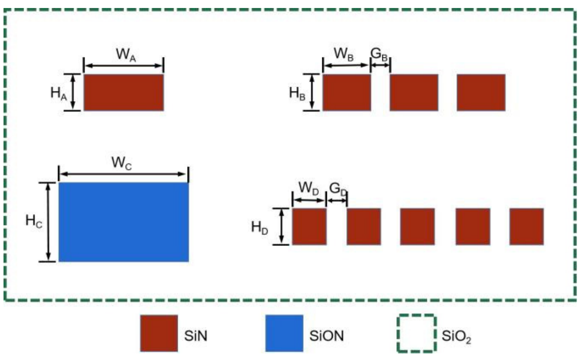

Figure 1. The structural diagrams of single-core SiN waveguide (top left), single-core SiON waveguide (bottom left), three-segment SiN waveguide (top right) and five-segment SiN waveguide (bottom right).

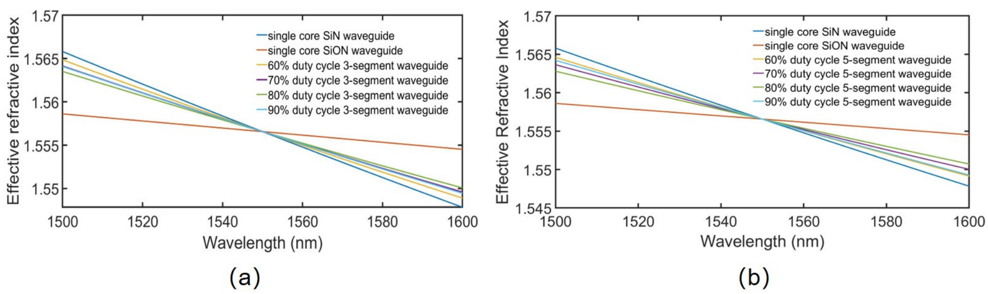

Figure 2. Dispersion curves of single-core SiN waveguide (1.2 μm × 0.25 μm), single-core SiON waveguide (3 μm × 1.8 μm) and (**a**) 60–90% duty cycle 3-segment SiN waveguides; (**b**) 60–90% duty cycle 5-segment SiN waveguides.

The schematic diagram of the broadband filter, comprised of single-core SiN and SiON waveguides, is presented in Figure 3. The SiN waveguide, which has a fixed thickness of 0.25 µm, is located below. In the upper end, there is the SiON waveguide, with a cross-sectional size of 3 µm × 1.8 µm. Both waveguides are surrounded by SiO_2. Instead of the traditional lateral coupling scheme in the adiabatic coupler, vertical coupling is employed here to ease the fabrication tolerance in terms of two aspects. Firstly, it eliminates the need for precise monitoring of the endpoint of the SiON waveguide etching to prevent damage to the SiN layer. Secondly, it allows for the creation of a small gap between the waveguides, where controlling the deposited SiO_2 thickness is easier and more cost-effective compared to improving the lithography resolution.

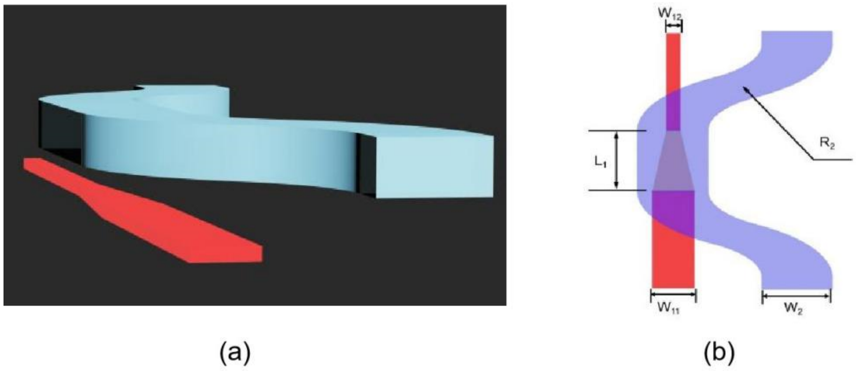

Figure 3. (**a**) Three-dimensional schematic diagram and (**b**) top view of the broadband filter with an adiabatic coupler.

Figure 4 illustrates the dispersion curves of SiON and SiN waveguides with varying widths. The taper part in the SiN waveguide, ranging from W_{11} to W_{12}, represents different matching wavelengths with the SiON waveguide, where light transfers between the two waveguides. In Figure 5, the supermode filed distributions are shown for the SiON and SiN composite waveguide with different SiN widths at a specific wavelength. Carefully designed SiN taper waveguide widths enable the creation of long-pass, short-pass, band-pass and band-stop filters within a specific wavelength range, as demonstrated in Figure 6. The transmittance spectra for different SiN taper waveguide widths are obtained through simulation using the wide-angle beam propagation method (BPM) method in Rsoft software. For instance, SiN waveguides with widths of 0.9 µm and 1.1 µm correspond to matching wavelengths of 1370 nm and 1490 nm, respectively. Thus, light within the 1370 nm to 1490 nm range transfers from one waveguide to the other across the adiabatic coupler. By analyzing the wavelength range of 1450 nm to 1650 nm and injecting light from the SiN waveguide, light below 1490 nm is emitted from the SiON waveguide, while light above 1490 nm remains in the SiN waveguide, resulting in a short-pass characteristic for the SiON waveguide and a long-pass characteristic for the SiN waveguide. In another example, SiN waveguides with widths of 1.05 µm and 1.25 µm correspond to matching wavelengths of 1470 nm and 1590 nm, respectively. Again, considering a wavelength range from 1450 nm to 1650 nm and injecting light from the SiN waveguide, light from 1470 to 1590 nm is emitted from the SiON waveguide, while light below 1470 nm and above 1590 nm remains in the SiN waveguide, resulting in a band-pass characteristic for the SiON waveguide and a band-stop characteristic for the SiN waveguide. To achieve the above filtering characteristics over a wider wavelength range, the widths at the starting and ending points of the SiN taper waveguide can be adjusted. Figure 7 presents the transmittance spectra of the adiabatic coupler with SiN taper widths ranging from 0.9 µm to 2.1 µm. The simulation results reveal its short-pass and long-pass characteristics over a large wavelength range from 0.8 µm to 1.9 µm.

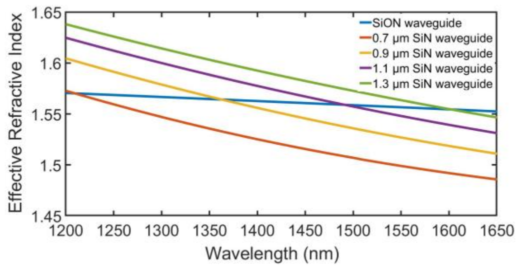

Figure 4. Dispersion curves of SiON and SiN waveguides with different widths.

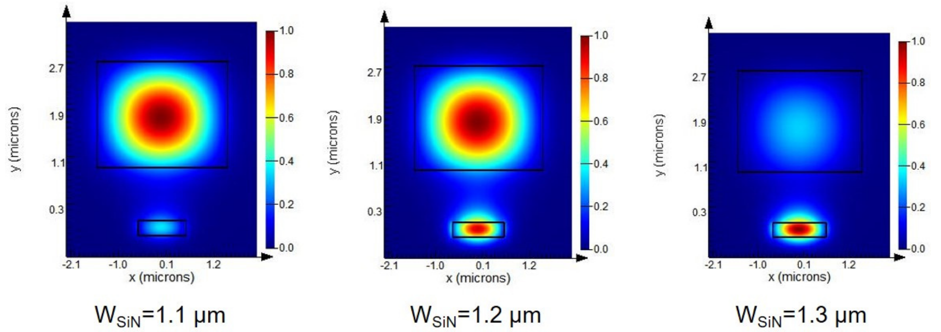

Figure 5. Supermode filed distributions for the SiON and SiN composite waveguide with different SiN widths at a specific wavelength. In the figure, the above is a SiON waveguide with a width of 3 μm and a height of 1.8 μm. The below is a SiN waveguide with a height of 0.25 μm.

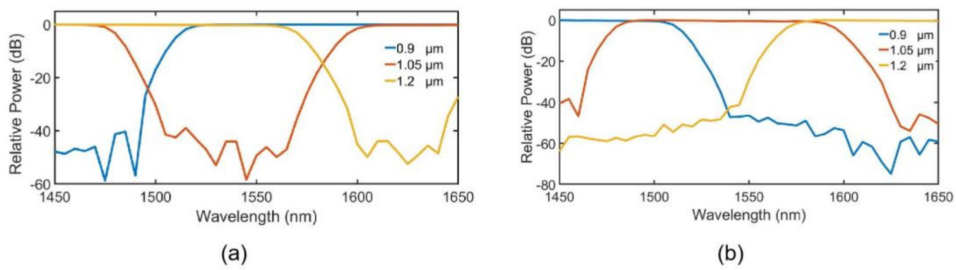

Figure 6. Transmittance spectra of the (**a**) SiN waveguide and (**b**) SiON waveguide with different W_{11} when light is injected into SiN waveguide. In all situations, W_{12} equals W_{11} + 0.2 μm.

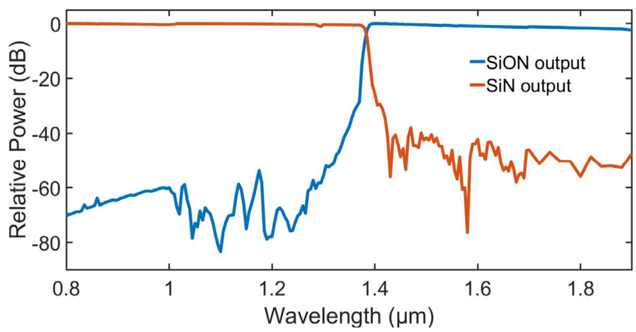

Figure 7. Simulated transmittance spectra of the adiabatic coupler when the SiN taper widths range from 0.9 μm to 2.1 μm. Light is injected from the SiN waveguide.

In addition to the pass or stop band width, the roll-off value and ER are the other two important parameters for broadband filters. The roll-off value, dependent on the slope difference of the dispersion curve, can be observed in Figure 6 and is approximately 1 dB nm^{-1} in our design. Meanwhile, ER is closely related to the length of the adiabatic coupler, which consists of the approaching part, coupling part, and separating part. In our structure, the length of the coupling part is denoted as L_1, while the lengths of the approaching and separating parts are determined by R_2, which is the radius of the S bends used in these sections. Figure 8 presents the relationship between ER and L_1, R_2. Generally, a longer length of the adiabatic coupler results in a larger ER. However, it is necessary to strike a balance between achieving a high ER and keeping the overall size of the structure small. Therefore, we have chosen a taper length for L_1 as 2000 µm and an R_2 value of 500,000 µm. The lateral distance between the centers of the SiN and SiON waveguides at the start and end points of the broadband filter is set to 5.5 µm to ensure that the two waveguides operate independently without any coupling or interference, as this would degrade the ER performance. The gap between the SiN and SiON waveguides has a minor impact on the filter performance as long as the value remains below 1.1 µm, given that the length of the coupling part L_1 is 2000 µm. To provide sufficient fabrication tolerance and avoid damaging the SiN layer during the SiON etching process, we have set the gap to 0.9 µm. It should be noted that as the gap decreases, L_1 can be shortened accordingly. The detailed design parameters of the broadband filter are listed in Table 1. Further simulation analysis illustrates that variations in W_{11}, W_2 and H_2 result in shifts of the cut-off wavelength at rates of 0.57 nm/nm, 0.06 nm/nm and 0.15 nm/nm, respectively. Additionally, a small variation of 0.001 in the refractive index of SiON can cause a 6 nm drift in the cut-off wavelength.

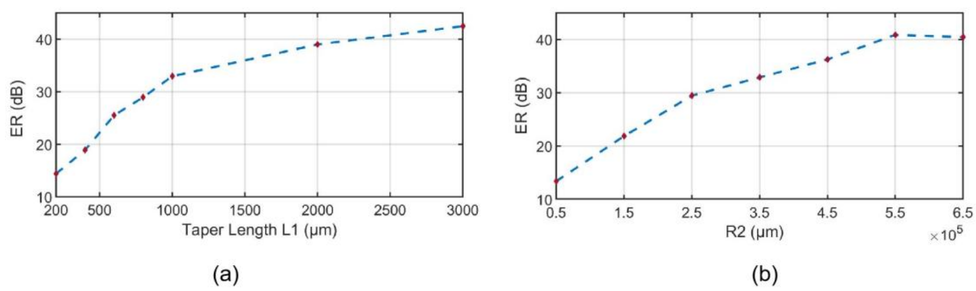

Figure 8. (**a**) The relationship between ER and taper length L_1 when R_2 is set to 500,000 µm and (**b**) the relationship between ER and R_2 when L_1 is set to 2000 µm. W_{11} and W_{12} of the taper waveguide are 1 µm and 1.2 µm, respectively, and the gap between the two waveguides is 0.9 µm. The red diamond is the measured discrete points and the blue dotted line is the connecting line between them.

Table 1. Detailed design parameters of the broadband filters in the 1550 nm band.

Parameters	Value (µm)	Parameters	Value (µm)	Parameters	Value (µm)
L_1	2000	W_{11}	0.8,0.85, 0.9, 0.95, 1.0, 1.05, 1.1, 1.15,1.2	Gap [a]	0.9
R_2	500,000			Distance [a]	5.5
H_1 [a]	0.25	W_2	2, 2.5, 3, 3.5, 4	W_{12}	W_{11} + 0.2
H_2 [a]	1.8			Total size	8650 × 10

[a] H_1 and H_2 represent the heights of SiN and SiON waveguides, respectively. Gap refers to the vertical gap between the SiN and SiON waveguides in the coupling area. Distance indicates the lateral distance between the centers of SiN and SiON waveguides at the start and end points of the broadband filter.

As mentioned in the introduction, SiN and SiON waveguides are transparent in the wavelength range from 300 nm to 2000 nm. A broadband filter with a sharp roll-off is desired not only in the 1550 nm band for the wideband WDM and multi-octave interferometry but also for applications such as fluorescence and Raman spectral analysis, where the excitation light in the visible band and near infra-red range (VNIR) needs to be filtered. Hence, we have designed a broadband filter with an adiabatic coupler comprising composite SiN and SiON waveguides operating in the 785 nm band. This filter can be utilized in an on-chip Raman spectrometer. The specific design parameters are listed in Table 2, and the simulated transmittance spectra of SiN and SiON waveguides are depicted in Figure 9. Similar to the 1550 nm band filter, a roll-off value of approximately 1 dB nm^{-1} can be observed in Figure 9. However, due to the unavailability of an appropriate light source in our lab for the 785 nm band, we have only fabricated and characterized the broadband filter in the 1550 nm band, as described in the subsequent sections, to first validate the feasibility of our device.

Table 2. Detailed design parameters of the broadband filters in the785 nm band.

Parameters	Value (μm)	Parameters	Value (μm)	Parameters	Value (μm)
L_1	3000	W_{11}	0.8	Distance	5.5
R_2	100,000	W_{12}	1.1		
H_1	0.25	W_2	1.6	Total size	5500 × 10
H_2	0.75	Gap	0.9		

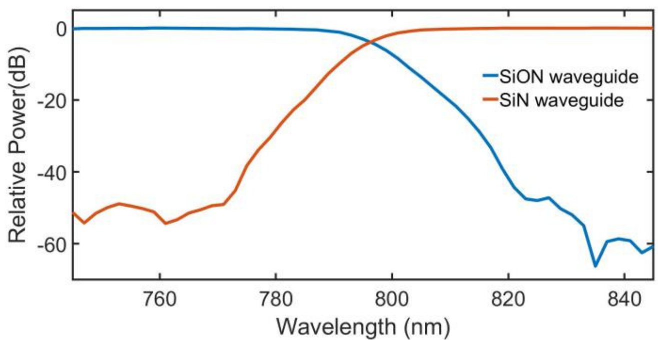

Figure 9. Transmittance spectra of the SiN and SiON waveguides in the 785 nm band.

3. Fabrication

Our device is fabricated on a commercial 4 inch, 250-nm-thick SiN wafer with an 8-μm-thick buried SiO_2 layer. To begin, a 1.2-μm-thick layer of AZ5214 photoresist is spin-coated onto the wafer at a speed of 3000 rpm. The photoresist is then exposed to 405 nm ultraviolet (UV) light at an intensity of 128 mJ/cm^2 using a SUSS MA6 lithography machine. After a 35-second development process, inductively coupled plasma (ICP) etching of the SiN layer is performed using an STS Multiplex ICP machine. Next, a 0.9-μm-thick layer of SiO_2 and a 1.8-μm-thick layer of SiON with a refractive index of 1.6 are deposited using an STS PECVD machine. To enhance the adhesion of the developed SiON film to the photoresist, a hydrophobic layer of CH_4, several nanometers thick, is formed on the SiON film using an Oxford ICP machine. Due to the considerable thickness of the SiON waveguide, we use a thick SPR220-4.5 photoresist as the mask for SiON etching to prevent any undesired deformations. The SPR220-4.5 is spun at a speed of 5500 rpm to create a 3.5 μm thick mask layer. A UV light intensity of 330 mJ/cm^2 and a 90-second development process are necessary to achieve clear development. The SiON layer is then etched using a reaction gas mixture of CHF_3 and CF_4. During the etching process, a balance between isotropic etching of F ion and the generation of fluorocarbon compounds that protect the sidewall is maintained to achieve a vertical profile [28]. This balance can be achieved by adjusting the gas flux ratio between CHF_3 and CF_4. Any residual fluorocarbon compound adhered to the waveguide is removed by immersing it in a hot solution of concentrated sulfuric acid (H_2SO_4) and aquae hydrogenii dioxidi (H_2O_2). Finally, a 6-μm-thick SiO_2 cover layer is deposited as both the upper cladding layer and the protection layer of the device. The entire fabrication process is illustrated in the flow-process diagram shown in Figure 10. Figure 11 displays a cross-section of the composite waveguides in the approaching area after SiON etching process. It should be noted that due to the similar conductivity of the SiN, SiON and SiO_2, the boundaries among these materials are not clearly distinguishable in the SEM image.

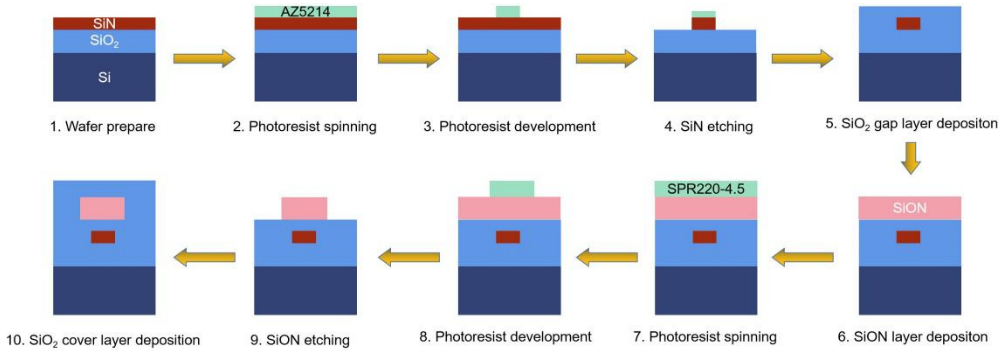

Figure 10. Flow process diagram of the entire fabrication process.

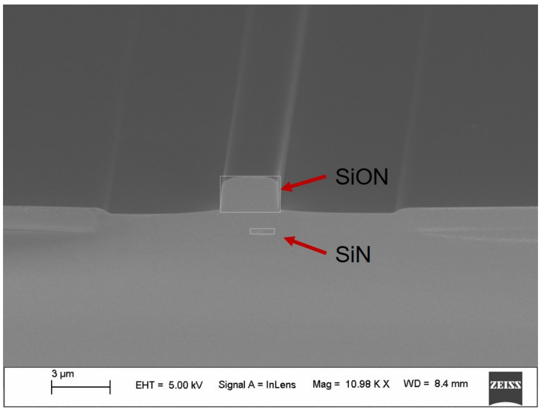

Figure 11. Cross-section of the composite waveguides in the approaching area after SiON etching process.

Tables 3 and 4 provide detailed procedures for the PECVD depositions of SiO_2, SiON, and ICP etchings of SiN, SiON. The precise control of the refractive index of the SiON film is crucial, as even minor variation can significantly shift the cut-off wavelength, as discussed earlier. The proportions of gas fluxes of SiH_4, N_2O and NH_3 have a significant impact on the refractive index of SiON [29]. Generally, a higher proportion of SiH_4 and NH_3 results in a higher refractive index. In our experiment, we kept the gas fluxes of SiH_4 and NH_3 fixed at 17.5 sccm and 190 sccm, respectively, and adjusted the N_2O flux to different values. The relationship between the measured refractive index of SiON and the N_2O flux is plotted in Figure 12. We conducted multiple measurements to ensure the stability of the refractive index of the developed SiON and observed a fluctuation of less than 0.0015, corresponding to a cut-off wavelength shift of 9 nm. On the other hand, the SiO_2 film is deposited with excessive N_2O flux, resulting in a highly stable refractive index that is largely unaffected by fluctuation in the chamber environment.

Table 3. Detailed procedures of the SiO_2 and SiON deposition using the STS PECVD machine.

Name	Pressure (mTorr)	Electrod Temperature (Degree)	RF Frequency (kHz)	RF Power (W)	SiH_4 Flux (sccm)	N_2O Flux (sccm)	NH_3 Flux (sccm)	Growth Rate (µm/min)
SiO_2	300	200 (upper) 150 (lower)	380	700	17.5	2000	0	0.163
SiON	300	200 (upper) 150 (lower)	380	700	17.5	250	190	0.106

Table 4. Detailed procedures of the SiN and SiON etching using the STS Multiplex ICP machine.

Name	Pressure (mTorr)	Coil Power (W)	Platen Power (W)	RF Frequency (MHz)	Wafer Temperature (Degree)	CHF_3 Flux (sccm)	CF_4 Flux (sccm)	Etching Rate (µm/min)
SiN	5	200	15	13.56	20	5.3	30.1	0.071
SiON	3	800	50	13.56	20	20	36	0.168

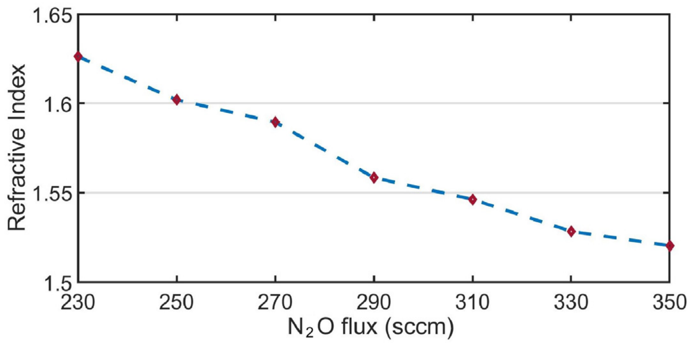

Figure 12. Relationship between the refractive index of the developed SiON and the N_2O flux when the SiH_4 and NH_3 fluxes is kept as 17.5 sccm and 190 sccm, respectively.

SiN and SiO_2 have a significant lattice mismatch, which can result in substantial stress. In the case of a commercially available SiN wafer with a buried SiO_2 layer, most of the stress has already been relieved. Therefore, developing the SiO_2 film directly on the complete SiN wafer would not cause noticeable stress-related issues. On the other hand, when fabricating the SiN waveguide, if a substantial portion of the SiN film is etched away, the stress will increase dramatically, leading to the formation of bulb-like defects during the subsequent SiO_2 deposition. To mitigate this, only a small area along the SiN waveguide is etched, ensuring that the majority of the SiN film remains intact, as illustrated in Figure 13. The separation distance between the SiN slab and the SiON waveguide is carefully designed to be 6.5 µm, providing sufficient space to avoid any coupling or interference between them. A micrograph of the fabricated broadband filter chip is shown in Figure 14, while Figure 15 displays SEM images of the adiabatic coupler at different positions. In the overlapping region of the SiON and SiN waveguides, a minor bump can be observed. However, this bump has a negligible impact on the overall performance of the filter due to the fact that the buried SiN waveguide has a very low height of only 250 nm, resulting in a limited height for the bump. Additionally, the bump formed very slowly as the two waveguides approached each other, minimizing any noticeable loss caused by mode-filed mismatch.

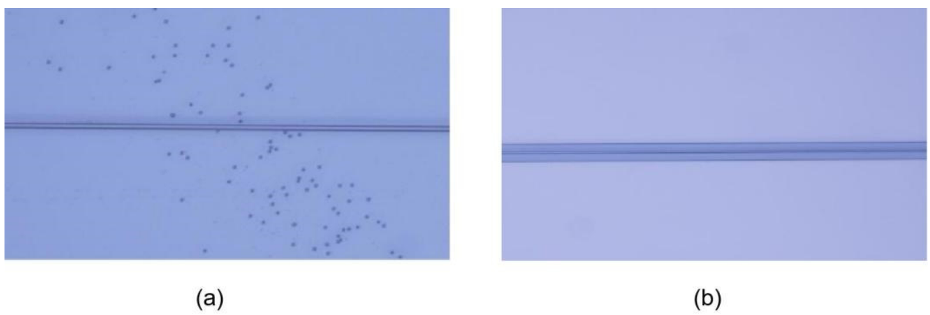

Figure 13. Micrographs of the SiN waveguide after SiO_2 and SiON layers have been deposited when (**a**) most of the SiN film on the wafer has been etched; (**b**) only SiN film near the waveguide has been etched.

Figure 14. Micrograph of the fabricated filter array with different parameters.

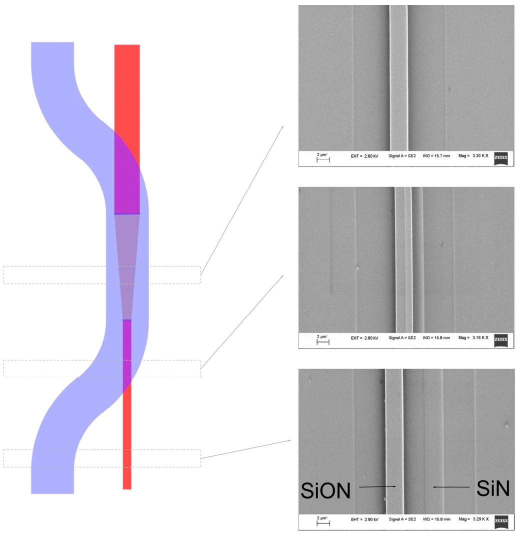

Figure 15. SEM images of the adiabatic coupler at different positions after SiON etching.

4. Characterization and Discussion

The fabricated broadband filter chip is characterized using a vacuum absorption supporting seat with two six-axis adjustable stages positioned on each side. An external-cavity tunable laser (Keysight 81606A, CA, USA) serves as the light source, emitting a laser within a wavelength range from 1500 nm to 1600 nm. After transmitting through a three-paddle polarization controller, the TE-polarized light enters the chip via a polarization-maintaining lensed fiber. At the output end of the chip, the light is collected by a multi-mode fiber and directed to a photodetector (Keysight 81634A, CA, USA).

Initially, we measured the propagation losses of SiN and SiON waveguides using the cut-back method. The SiN waveguide, with dimensions of 1.2 μm × 0.25 μm, has a propagation loss of 2.7 dB/cm, mainly attributed to scattering loss caused by sidewall roughness. The 3 μm × 1.8 μm SiON waveguide experiences a significantly higher propagation loss of 9.6 dB/cm due to the presence of trich N-H bonds in the film. The propagation loss related to N-H bonds can be reduced by using hydrogen-free gas SiD4 instead of SiH4 during SiON deposition via PECVD. This has been shown to achieve a propagation loss of 0.29 dB/cm at 1550 nm [29]. Additionally, the coupling losses of SiN and SiON waveguides are measured to be 6.9 dB and 2.8 dB, respectively.

Considering the larger propagation loss of the SiON waveguide, we inject light from the input end of the SiN waveguide. Figure 16 presents the normalized transmittance spectrum at the output ends of the SiN and SiON waveguides for two adjacent filters, with the influence of coupling loss already deducted. From Figure 16, it can be observed that filter 1 and filter 2 exhibit a 30 nm cut-off wavelength shift due to the 0.05 μm difference in SiN taper width, which aligns well with our simulations. The long-pass spectra obtained from the SiN waveguide output demonstrate an ER larger than 15 dB. Conversely, the low-pass spectra collected from the SiON waveguide exhibit a smaller ER of approximately 12 dB and an excess insertion loss of over 3.5 dB. This is primarily a result of the higher propagation loss in the SiON waveguide. In all the output ends of the two filters, the roll-off values in the transition edges are measured to be larger than 0.7 dB nm^{-1}. The deviation of the cut-off wavelength from the designed value is due to fluctuations in refractive index and waveguide cross-sectional size. A red shift of 15 nm is observed in the transmittance spectra. Assuming the waveguide height matches the designed value, the observed 0.1 µm reduction in SiON waveguide width can account for a 6 nm red shift. The remaining 9 nm shift can be attributed to the refractive index fluctuation of SiON, which amounts to 0.0015. This estimation is based on the analysis results of fabrication tolerance discussed in the Section 2. To achieve an accurate cut-off wavelength, future work can introduce materials with large thermo-optic or electro-optic coefficients as cladding layers. Misalignment between the two layers can result in an increase in the gap width between them. However, as we have analyzed in the Section 2 when employing the vertical coupling and with a designed gap of 0.9 µm, a 1 µm lateral misalignment would only lead to a 0.25 µm increase in gap width. Moreover, if the length of the coupling part L_1 is 2000 µm, the gap between the SiN and SiON waveguides has a minor impact on the filter performance as long as it remains below 1.1 µm. Therefore, misalignment between the two layers will not significantly degrade the performance of our filter chip.

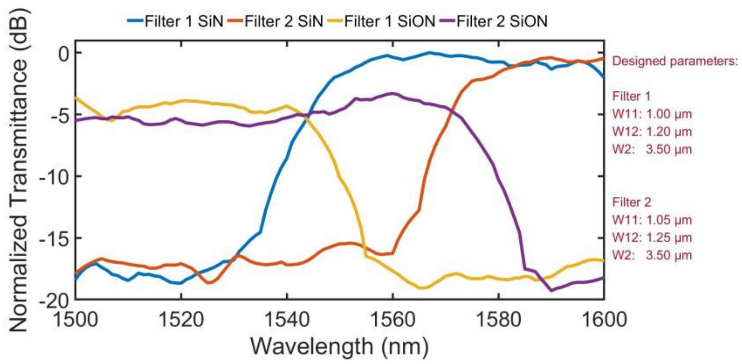

Figure 16. Normalized transmittance spectra in the output ends of the SiN and SiON waveguides in two adjacent filters.

Compared to previous work with the classical adiabatic coupler, the roll-off value of 0.7 dB nm^{-1} in our work demonstrates a significant improvement. The adiabatic coupler made up of a single-core and a three-segment silicon waveguide exhibits a larger roll-off value of 2.82 dB nm^{-1} in the 1550 nm band. However, the application of silicon in the visible and short infra-red bands is limited by its 1100 nm absorption edge. SiN, on the other hand, holds great promise in these bands due to its high transparency, large refractive index and reliable stability. The SiN and SiON composite waveguide coupler employed in this study demonstrates superiority in achieving a higher roll-off value compared to the multi-segment SiN waveguide structure. Additionally, the vertical coupling method employed simplifies fabrication and proves its feasibility. Therefore, the SiN and SiON composite waveguide coupler is one of the most promising structures for constructing a broadband filter with sharp transition edges, especially in the wavelength range extending below 1100 nm.

5. Conclusions

In summary, we have presented the design, fabrication and characterization of a broadband filter with sharp transition edges based on an adiabatic coupler. By tuning the taper waveguide width, the bandwidth can be conveniently tuned, allowing for flexible switching between long-pass, short-pass, band-pass and band-stop filters within a specific wavelength range. The SiN and SiON composite waveguide employed in this study exhibits wide applicability and can cover wavelengths from the ultraviolet to the infrared bands. Although the presence of N-H bonds in the SiON waveguide results in a large propagation loss and reduces the filter's ER, this issue can be effectively eliminated by using hydrogen-free gas SiD_4 in the PECVD deposition process. Further improvement in the ER can be achieved through cascading filters and refining the fabrication process to reduce scattering losses.

Author Contributions: Conceptualization, X.M.; methodology, X.M. and Q.S.; simulation, X.M. and J.G.; validation, J.-J.H. and T.L.; fabrication, X.M. and Q.S.; data curation, X.M.; writing—original draft preparation, X.M.; writing—review and editing, X.G.; visualization, X.M.; supervision, J.-J.H.; project administration, X.M. All authors have read and agreed to the published version of the manuscript.

Funding: This work was completed with help from the Zhejiang Provincial Natural Science Foundation of China under Grant No.LQ21F050003 and Research Start-up Funds of Zhejiang University of Science and Technology.

Informed Consent Statement: Not applicable.

Data Availability Statement: The data presented in this study are available upon request from the corresponding author. The data are not publicly available.

Conflicts of Interest: The authors declare no conflict of interest.

References

1. Takashina, S.; Mori, Y.; Hasegawa, H.; Sato, K.-I.; Watanabe, T. Wavelength-tunable filters utilizing arrayed waveguide gratings for colorless/directionless/contentionless optical signal drop in ROADMs. *IEEE Photonics J.* **2015**, *7*, 1–11. [CrossRef]
2. Wang, Y.; Chen, D.; Zhang, G.; Wang, J.; Tao, S. A super narrow band filter based on silicon 2D photonic crystal resonator and reflectors. *Opt. Commun.* **2016**, *363*, 13–20. [CrossRef]
3. Prabhu, A.M.; Tsay, A.; Han, Z.; Van, V. Ultracompact SOI microring add–drop filter with wide bandwidth and wide FSR. *IEEE Photonics Technol. Lett.* **2009**, *21*, 651–653. [CrossRef]
4. Xiong, K.; Xiao, X.; Li, X.; Hu, Y.; Li, Z.; Chu, T.; Yu, Y.; Yu, J. CMOS—Compatible reconfigurable microring demultiplexer with doped silicon slab heater. *Opt. Commun.* **2012**, *285*, 4368–4371. [CrossRef]
5. Tyndall, N.F.; Stievater, T.H.; Kozak, D.A.; Pruessner, M.W.; Holmstrom, S.A.; Rabinovich, W.S. Ultrabroadband lattice filters for integrated photonic spectroscopy and sensing. *Opt. Eng.* **2018**, *57*, 127103. [CrossRef]
6. Shen, A.; Qiu, C.; Yang, L.; Dai, T.; Li, Y.; Yu, H.; Hao, Y.; Jiang, X.; Yang, J. Tunable microring based on-chip interrogator for wavelength-modulated optical sensors. *Opt. Commun.* **2015**, *340*, 116–120. [CrossRef]
7. Maru, K.; Fujii, Y. Reduction of chromatic dispersion due to coupling for synchronized-router-based flat-passband filter using multiple-input arrayed waveguide grating. *Opt. Express* **2009**, *17*, 22260–22270. [CrossRef]
8. Li, J.; Yin, R.; Ji, W.; Huang, Q.; Gong, Z.; Lv, L.; Zhou, X. AWG optical filter with tunable central wavelength and bandwidth based on LNOI and electro-optic effect. *Opt. Commun.* **2020**, *454*, 124445. [CrossRef]
9. Chatterjee, A.; Selvaraja, S.K. On-chip silicon nano-slab photodetector integrated wavelength division de-multiplexer in the 850 nm band. *Appl. Opt.* **2022**, *61*, 1403–1412. [CrossRef]
10. Ren, Y.; Jiang, Z.; Van, V. A General variable bandwidth microring filter for lossless bandwidth tuning. *J. Light. Technol.* **2021**, *39*, 4745–4751. [CrossRef]
11. Jiang, L.; Shi, L.; Luo, J.; Gao, Q.; Lan, T.; Huang, L.; Zhu, T. Narrow linewidth VCSEL based on resonant optical feedback from an on-chip microring add-drop filter. *Opt. Lett.* **2021**, *46*, 2320–2323. [CrossRef] [PubMed]
12. Liu, P.; Zheng, P.; Yang, H.; Lin, D.; Hu, G.; Yun, B.; Cui, Y. Parity-time symmetric frequency-tunable optoelectronic oscillator based on a Si_3N_4 microdisk resonator. *Appl. Opt.* **2021**, *60*, 1930–1936. [CrossRef] [PubMed]
13. Pimbi, D.; Hasan, M.; Mia, B.; Jaidye, N.; Kim, S. Polarization-independent photonic Bragg grating filter with cladding asymmetry. *Opt. Lett.* **2023**, *48*, 1192–1195. [CrossRef]
14. Oser, D.; Pérez-Galacho, D.; Le Roux, X.; Tanzilli, S.; Vivien, L.; Labonté, L.; Cassan, É.; Alonso-Ramos, C. Silicon subwavelength modal Bragg grating filters with narrow bandwidth and high optical rejection. *Opt. Lett.* **2020**, *45*, 5784–5787. [CrossRef]
15. Kim, J.Y.; Cho, H.J.; Do, Y.S. High color purity plasmonic color filter by one-dimensional photonic crystals. *Nanomaterials* **2022**, *12*, 1694. [CrossRef]
16. Kohli, N.; Sang, B.L.; Nabki, F.; Menard, M. Tunable Bandpass Filter With Serially Coupled Ring Resonators Assisted MZI. *IEEE Photonics J.* **2021**, *13*, 1–8. [CrossRef]
17. Saha, N.; Brunetti, G.; Armenise, M.N.; Ciminelli, C. Tunable narrow band add-drop filter design based on apodized long period waveguide grating assisted co-directional coupler. *Opt. Express* **2022**, *30*, 28632–28646. [CrossRef]
18. Chen, P.; Chen, S.; Guan, X.; Shi, Y.; Dai, D. High-order microring resonators with bent couplers for a box-like filter response. *Opt. Lett.* **2014**, *39*, 6304–6307. [CrossRef]

19. Xu, H.; Dai, D.; Shi, Y. Low-crosstalk and fabrication-tolerant four-channel CWDM filter based on dispersion-engineered Mach-Zehnder interferometers. *Opt. Express* **2021**, *29*, 20617–20631. [CrossRef]
20. Gong, Z.; Ji, W.; Yin, R.; Li, J.; Song, Z. Tunable microwave photonic filter based on LNOI polarization beam splitter and waveguide grating. *IEEE Photonics Technol. Lett.* **2020**, *32*, 787–790. [CrossRef]
21. Zhu, Y.; Zhou, Y.; Wang, Z.; Fang, Z.; Liu, Z.; Chen, W.; Wang, M.; Zhang, H.; Cheng, Y. Electro-optically tunable microdisk laser on Er^{3+}-doped lithium niobate thin film. *Chin. Opt. Lett.* **2022**, *20*, 011303. [CrossRef]
22. Zheng, S.N.; Zou, J.; Cai, H.; Song, J.F.; Chin, L.K.; Liu, P.Y.; Lin, Z.P.; Kwong, D.L.; Liu, A.Q. Microring resonator-assisted Fourier transform spectrometer with enhanced resolution and large bandwidth in single chip solution. *Nat. Commun.* **2019**, *10*, 2349. [CrossRef]
23. Menchon-Enrich, R.; Llobera, A.; Vila-Planas, J.; Cadarso, V.J.; Mompart, J.; Ahufinger, V. Light spectral filtering based on spatial adiabatic passage. *Light. Sci. Appl.* **2013**, *2*, e90. [CrossRef]
24. Stanton, E.J.; Heck, M.J.R.; Bovington, J.; Spott, A.; Bowers, J.E. Multi-octave spectral beam combiner on ultra-broadband photonic integrated circuit platform. *Opt. Express* **2015**, *23*, 11272–11283. [CrossRef] [PubMed]
25. Xu, X.-B.; Guo, X.; Chen, W.; Tang, H.X.; Dong, C.-H.; Guo, G.-C.; Zou, C.-L. Flat-top optical filter via the adiabatic evolution of light in an asymmetric coupler. *Phys. Rev. A* **2019**, *100*, 023809. [CrossRef]
26. Gorgulu, K.; Magden, E.S. Ultra-broadband integrated optical filters based on adiabatic optimization of coupled waveguides. *J. Light. Technol.* **2023**, *41*, 5067–5077. [CrossRef]
27. Magden, E.S.; Li, N.; Raval, M.; Poulton, C.V.; Ruocco, A.; Singh, N.; Vermeulen, D.; Ippen, E.P.; Kolodziejski, L.A.; Watts, M.R. Transmissive silicon photonic dichroic filters with spectrally selective waveguides. *Nat. Commun.* **2018**, *9*, 3009.
28. Oehrlein, G.S.; Matsuo, P.J.; Doemling, M.F.; Rueger, N.R.; Kastenmeier, B.E.E.; Schaepkens, M.; Standaert, T.; Beulens, J.J. Study of plasma—Surface interactions: Chemical dry etching and high-density plasma etching. *Plasma Sources Sci. Technol.* **1996**, *5*, 193–199. [CrossRef]
29. Hiraki, T.; Aihara, T.; Nishi, H.; Tsuchizawa, T. Deuterated SiN/SiON waveguides on Si platform and their application to C-band WDM filters. *IEEE Photonics J.* **2017**, *9*, 1–7. [CrossRef]